

A caspase-3 ‘death-switch’ in colorectal cancer cells for induced and synchronous tumor apoptosis *in vitro* and *in vivo* facilitates the development of minimally invasive cell death biomarkers

KL Simpson¹, C Cawthorne², C Zhou¹, CL Hodgkinson¹, MJ Walker^{1,3}, F Trapani¹, M Kadirvel², G Brown², MJ Dawson¹, M MacFarlane⁴, KJ Williams², AD Whetton³ and C Dive^{*1}

Novel anticancer drugs targeting key apoptosis regulators have been developed and are undergoing clinical trials. Pharmacodynamic biomarkers to define the optimum dose of drug that provokes tumor apoptosis are in demand; acquisition of longitudinal tumor biopsies is a significant challenge and minimally invasive biomarkers are required. Considering this, we have developed and validated a preclinical ‘death-switch’ model for the discovery of secreted biomarkers of tumour apoptosis using *in vitro* proteomics and *in vivo* evaluation of the novel imaging probe [¹⁸F]ML-10 for non-invasive detection of apoptosis using positron emission tomography (PET). The ‘death-switch’ is a constitutively active mutant caspase-3 that is robustly induced by doxycycline to drive synchronous apoptosis in human colorectal cancer cells *in vitro* or grown as tumor xenografts. Death-switch induction caused caspase-dependent apoptosis between 3 and 24 hours *in vitro* and regression of ‘death-switched’ xenografts occurred within 24 h correlating with the percentage of apoptotic cells in tumor and levels of an established cell death biomarker (cleaved cytokeratin-18) in the blood. We sought to define secreted biomarkers of tumor apoptosis from cultured cells using Discovery Isobaric Tag proteomics, which may provide candidates to validate in blood. Early after caspase-3 activation, levels of normally secreted proteins were decreased (e.g. Gelsolin and Midkine) and proteins including CD44 and High Mobility Group protein B1 (HMGB1) that were released into cell culture media *in vitro* were also identified in the bloodstream of mice bearing death-switched tumors. We also exemplify the utility of the death-switch model for the validation of apoptotic imaging probes using [¹⁸F]ML-10, a PET tracer currently in clinical trials. Results showed increased tracer uptake of [¹⁸F]ML-10 in tumours undergoing apoptosis, compared with matched tumour controls imaged in the same animal. Overall, the death-switch model represents a robust and versatile tool for the discovery and validation of apoptosis biomarkers.

Cell Death and Disease (2013) 4, e613; doi:10.1038/cddis.2013.137; published online 2 May 2013

Subject Category: Cancer

Evasion of apoptosis is a hallmark of cancer,¹ and consequently, re-initiating selective tumor cell death is a principal goal in anticancer drug development. This may be achieved by exploiting signalling pathways that control cell survival or initiate cell death, which are commonly deregulated in tumors.² Substantial effort is focused on novel agents designed specifically to activate pro-apoptotic signalling and overcome the anti-apoptotic molecular ‘roadblocks’ that allow tumor cells to survive in harsh microenvironments and resist current therapies.³ Examples include drugs targeted to anti-apoptotic Bcl-2 family proteins and to inhibitors of apoptosis (IAP) proteins and activators of the TRAIL death receptor signalling pathway.²

In parallel to drug development,¹ there is a clear requirement for biomarkers of tumor cell death applicable during early clinical trials. The acquisition of tumor tissue pre- and post-drug treatment is challenging whereas less invasive, serial blood sampling is commonplace. Similarly, imaging approaches offer the prospect of the assessment of cell death non-invasively. Our aim therefore was to develop a robust and versatile model system to facilitate discovery of novel biomarkers via these complimentary approaches. In the first instance, we sought identification of novel pharmacodynamic biomarkers *in vitro* that could potentially inform on and quantify drug-induced apoptosis in the circulation of cancer patients. It is likely that a ‘tumor cell death signature’ will have

¹Clinical and Experimental Pharmacology Group, Paterson Institute for Cancer Research, University of Manchester and Manchester Cancer Research Centre, Wilmslow Road, Withington, Manchester, UK; ²Wolfson Molecular Imaging Centre, University of Manchester, 27 Palatine Road, Manchester, UK; ³Stem Cell and Leukaemia Proteomics Laboratory, School of Cancer and Enabling Sciences, University of Manchester, Manchester Academic Health Science Centre, Christie Hospital, Manchester, UK and ⁴MRC Toxicology Unit, Hodgkin Building, University of Leicester, Lancaster Road, Leicester, UK

*Corresponding author: C Dive, Clinical and Experimental Pharmacology Group, Paterson Institute for Cancer Research, University of Manchester and Manchester Cancer Research Centre, Wilmslow Road, Withington, Manchester M20 4BX, UK. Tel: +44 (0)161 446 3036; Fax: +44 (0)161 446 3109; E-mail: CDive@PICR.man.ac.uk

Keywords: biomarkers; apoptosis; caspase-3; death-switch; proteomics; imaging

Abbreviations: cCK18, caspase-cleaved cytokeratin-18; CK18, cytokeratin-18; cC3, cleaved caspase-3; cPARP, cleaved PARP; CRC, colorectal cancer; HMGB1, High Mobility Group Protein B1; Hsp90, Heat Shock Protein 90; iTRAQ, isobaric tagging for relative and absolute quantification; MALDI-TOF, matrix-assisted laser desorption ionisation-time of flight; MS, mass spectrometry; PET, positron emission tomography; RPLC, reverse phase liquid chromatography

Received 06.11.12; revised 22.2.13; accepted 25.2.13; Edited by A Stephanou

increased power and sensitivity over a single biomarker. The use of an unbiased global approach may also increase understanding of the apoptosis process in tumor cells *per se*. We also sought to demonstrate proof-of-principle that our cell death model would have utility for the preclinical validation of imaging biomarkers of apoptosis that are translatable to the clinic.

Apoptosis culminates in activation of caspases (initiator caspases cleave and activate downstream effector caspases), a family of cysteine proteases primarily responsible for orchestrating the demolition of key cellular structures and the subsequent engulfment of apoptotic corpses by phagocytes.^{4–6} Hundreds of proteins undergo restricted proteolysis by effector caspases,⁷ resulting in a myriad of changes in the proteome. Effector caspase activation is therefore stringently regulated. The preclinical model developed here (referred to as the ‘death-switch’) exploits the convergence of apoptotic signalling pathways on caspase-3 and relies on the tightly controlled, doxycycline-inducible activation of a constitutively active mutant of caspase-3 (or an inactive point mutant)⁸ to drive synchronous apoptosis in HT29 colorectal cancer (CRC) cells. Here, there is no reliance upon upstream, potentially confounding signalling events and apoptosis irrevocably occurs when the active protein is inducibly expressed. CRC is the third most common cancer type worldwide according to the GLOBOCAN 2008 Cancer Incidence and Mortality Worldwide Database (<http://globocan.iarc.fr>) and thus warrants further study. However, the death-switch approach is applicable to any readily transfectable tumour cell line.

Changes in both intracellular and secreted/released proteins after synchronous induction of the death-switch are measurable both *in vitro* and *in vivo* using human tumor xenograft models allowing correlative assessment of apoptosis in the tumor and in the bloodstream. In this study, the ‘death-switch’ model was used *in vitro* to examine biomarkers of apoptosis via a mass-spectrometry (MS)-based global proteomic approach and to demonstrate utility in the preclinical validation of apoptotic imaging agents using PET [¹⁸F]ML-10, a PET tracer currently undergoing clinical trials in oncology.^{9,10}

Results

Generation of a HT29 human CRC cell line that undergoes tightly regulated, rapid and synchronous apoptosis. To investigate the kinetics of tumor apoptosis *in vivo* and the resultant proteomic changes, it was necessary to generate a model whereby apoptosis induction was tightly controlled and synchronous. RevC3 and revC3 C/A constructs⁸ were subcloned into the pTRE2hyg vector, which permits their expression only in the presence of doxycycline (dox). Vectors were transfected into the HT29 CCE9 parental cell line¹¹ in order to generate revC3 (death-switch) and revC3 C/A (inactive point mutant) clones. Clones were selected based on expression of revC3 and revC3 C/A and their ability upon dox exposure to exhibit functional and morphological characteristics of apoptosis (Figure 1). Expression was monitored using a caspase-3 antibody directed towards D175 of the large subunit, normally

exposed only under conditions of endogenous caspase-3 cleavage (and undetectable in the full-length pro-enzyme), which due to the generation of either revC3 or revC3 C/A due to subunit rearrangement is present at the C-terminus of these proteins. RevC3 (Figure 1a(i)) and revC3 C/A (Figure 1a(ii)) were rapidly and continually induced from 3–24 h after dox. Overexpression of revC3 generated the p19 large subunit of caspase-3 after 4 h (increased at 6 h) and cleavage of an established caspase-3 substrate, PARP, while overexpressed revC3 C/A was catalytically inactive, confirmed by the absence of PARP cleavage. Although in the case of revC3 C/A a small amount of the p19 subunit was detectable after 6 h, this did not generate catalytically active protein (shown by the lack of cleaved PARP). Furthermore, PARP cleavage by revC3 (in addition to generation of the p19 subunit) was inhibited by the pan-caspase inhibitor, Boc-D-FMK (Figure 1a(i)), indicating a specific caspase-driven apoptotic effect.

While cells in the absence of revC3 (Figure 1b(i)) or in presence or absence of revC3 C/A (Figure 1b(ii)) expression displayed the same growth kinetics *in vitro* as the parental cell line, dox induction of revC3 rendered cells non-viable within 24 h (Figure 1b(i)). These data demonstrate that revC3 expression induced a ‘non-leaky’ cell death, indicative of a robust model system. Expression of the transgene *per se* is not detrimental to cells, as shown by revC3 C/A expression.

The functional and morphological characteristics of cells upon induction of revC3 were consistent with apoptosis, in comparison to revC3 C/A-expressing cells (Figure 1c). Caspase activity after 6 h of dox exposure was significantly higher in revC3 cells compared with revC3 C/A cells ($P < 0.001$) (Figure 1c(i)) and was quenched by the addition of caspase-3 inhibitor DEVD, indicating a caspase-3 dependence. After 24 h of caspase activation in revC3 cells, caspase activity was reduced to baseline, which when correlated with cell viability (Figure 1c(ii)) was consistent with ~50% of these cells being rendered non-viable ($P \leq 0.03$ versus all other groups). After 6 h, 73% of revC3-expressing cells in the presence of dox exhibited classical nuclear apoptotic morphology (nuclear condensation/fragmentation) in comparison to <5% of revC3 cells in the absence of dox and revC3 C/A cells regardless of dox (Figure 1c(iii)). Taken together, the data show that induction of the death-switch provokes rapid, synchronous expression and activation of caspase-3 and subsequent apoptosis.

Expression of revC3 in tumors leads to rapid, synchronous apoptosis *in vivo*, which correlates with tumor regression, tumor apoptosis and circulating levels of cytokeratin-18. Selective expression of the death-switch or the inactive point mutant in tumors *in vivo* was obtained by dosing tumor-bearing mice with dox by oral gavage every 24 h, after tumors reached a volume of 800 mm³. Tumor growth kinetics are shown in Figure 2a. In the absence of dox, revC3-containing xenografts (Figure 2a(ii)) displayed the same growth kinetics (not significantly different: two-way analysis of variance (ANOVA)) as the revC3 C/A cells, both in the presence and absence of dox (Figures 2a(iii) and (iv), respectively) throughout the experiment. Following dox, a marked tumor regression

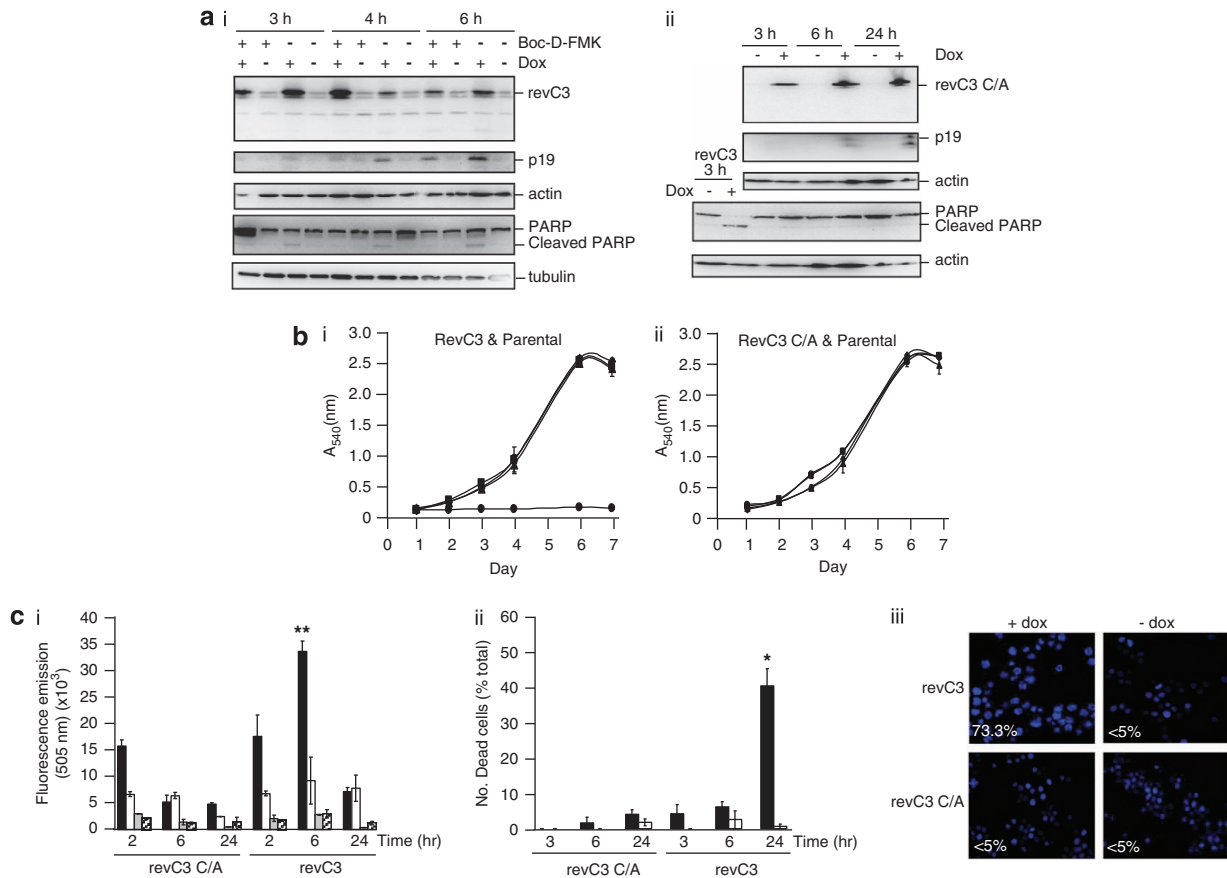


Figure 1 Validation of the death-switch *in vitro*. (a) Levels of revC3, endogenous cleaved caspase-3, p19 large subunit of cleaved caspase-3 and PARP in revC3-expressing \pm Boc-D-FMK (1 mM) (i) or revC3 C/A (ii) cells \pm dox, for 3, 4, 6 or 24 h. Lysates were probed for expression and processing as an indicator of apoptosis. Loading controls are actin and tubulin. Data shown are representative of three independent experiments. The large p19 subunit of caspase-3 (generated by cleavage of the pro-enzyme) is denoted by 'p19'. (b) Cell population growth kinetics of revC3 and parental HT29 CCE9 cells (i) and revC3 C/A and parental HT29 CCE9 (ii) cells \pm dox daily for 7 days. (i) RevC3 + dox (\bullet), revC3 - dox (\blacksquare), HT29 CCE9 + dox (\blacktriangle), HT29 CCE9 - dox (\blacklozenge). (ii) revC3 C/A + dox (\bullet), revC3 C/A - dox (\blacksquare), HT29 CCE9 + dox (\blacktriangle), HT29 CCE9 - dox (\blacklozenge). Data shown are the mean of $n = 3 \pm$ SD. (c) Kinetics of caspase-3 activity by fluorometric caspase-3 assay of revC3- and revC3 C/A-expressing cells \pm dox, \pm DEVD-CHO (i). (ii) Changes in cell viability in revC3- versus revC3 C/A-expressing cells \pm dox. (iii) Nuclear morphology of revC3 and revC3 C/A cells \pm dox for 6 h, % number of cells with apoptotic nuclear morphology. Solid black bars, + dox; open white bars, - dox; light grey bars, + dox, + DEVD-CHO; hashed bars, - dox, + DEVD-CHO. Data shown are mean of $n = 3 \pm$ SEM. ****** $P < 0.001$ versus C/A 6 h. ***** $P < 0.003$ versus all other groups

occurred in revC3 xenografts by 24 h (Figure 2a(i)), with tumor shrinkage to $\sim 50\%$ of original size by 48 h dox (two-way ANOVA followed by Student–Neuman–Keuls test, $P < 0.001$; Figure 2a(v)).

In revC3 xenografts, there were substantial increases in the number of cells that stained positively for all three apoptotic biomarkers (Figure 2b(i), quantitated in (ii)) (cPARP, 54.8%, $P < 0.001$; cC3, 20.9%, $P < 0.001$; caspase-cleaved CK18 (cCK18), 21.6%, $P < 0.02$; revC3 + dox versus all other groups). Differences in the proportion of cells that stained positive for each marker may be attributed to the quality of the antibody, in combination with the timing of the sample; for example, cC3 may appear earlier and be more rapidly degraded than cPARP. There was a maximum of 11% apoptotic cells in tumors (cCK18) either not exposed to dox or where the inactive point mutant replaced RevC3 (Figure 2b(ii)). Significant differences were observed in tumor volume and cPARP as early as 3 h post dox (compared with mice not receiving dox), whereas cC3 levels were significantly

increased by 8 h and cCK18 by 24 h ($P < 0.02$ in all cases) (Figure 2b(iii)).

The M65 ELISA measures levels of human full-length and caspase-cleaved CK18 (cCK18), giving an indication of the amount of total cell death occurring in epithelial cells,¹² while the M30 ELISA measures the levels of cCK18 only and thus reports epithelial cell apoptosis.^{13,14} These ELISAs have poor affinity for mouse CK18. In agreement with tumor biomarker data (Figure 2b), circulating CK18 in revC3 xenografts 24 h after dox was significantly elevated compared with all other groups and also correlated with tumor regression ($P < 0.01$) (Figure 2c(i)). Furthermore, the agreement between M65 and M30 data inferred that the predominant mode of induced cell death was apoptosis. While tumor volumes were significantly decreased from 3 h compared with tumors prior to dox ($P < 0.01$), M30/M65 levels became significantly elevated from 8 h ($P < 0.01$) (Figure 2c(ii)). Together, these data validate the death-switch model as a robust *in vivo* model of regulated, synchronous apoptosis and with the kinetics of

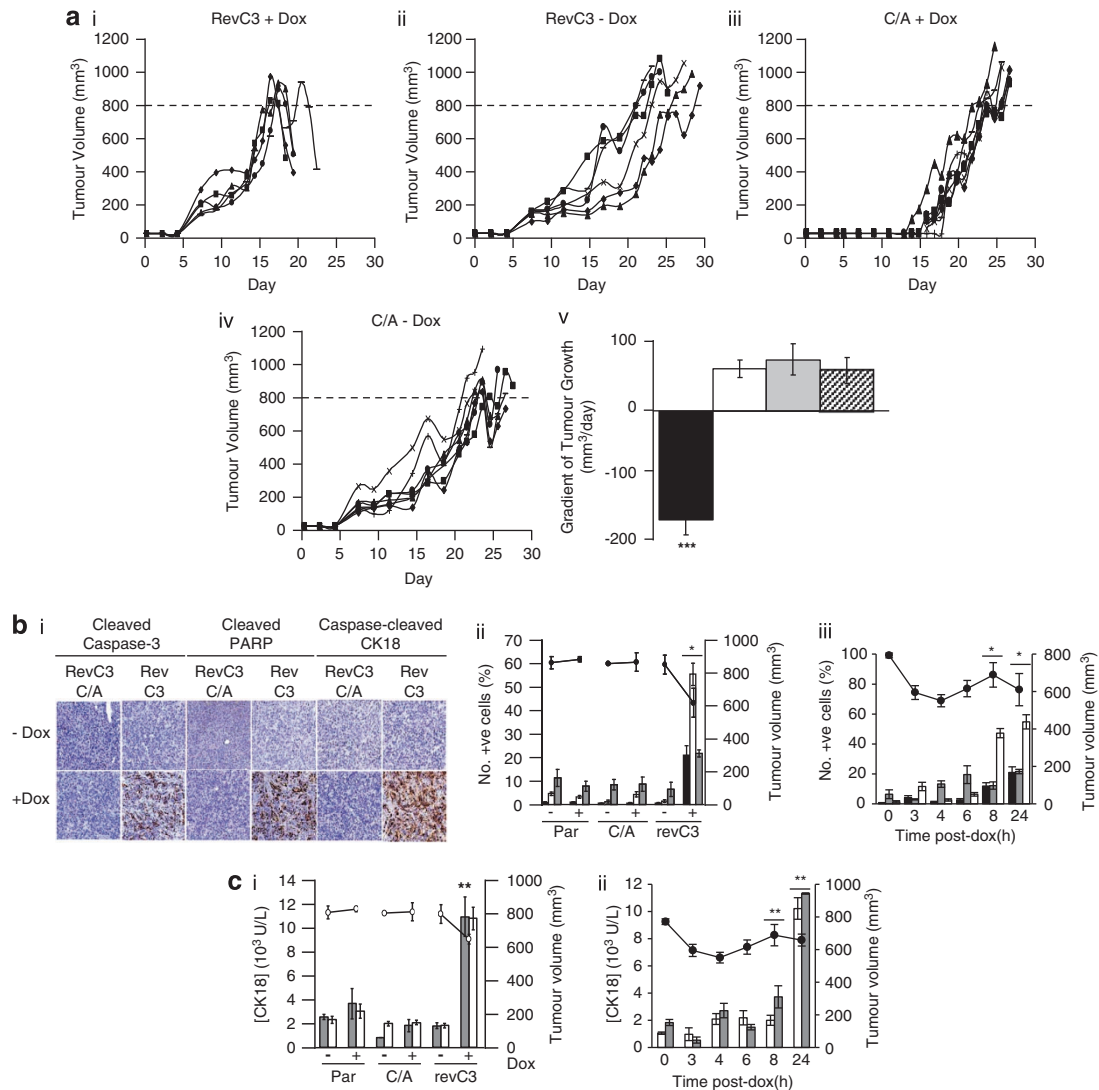


Figure 2 Validation of the death-switch *in vivo*. (a) Changes in tumor volume \pm dox for individual SCID/*bg* mice bearing RevC3 or C/A xenografts (i–iv). (i) RevC3-bearing animals + dox gavage, (ii) RevC3-bearing animals + control (water) gavage, (iii) C/A-bearing animals + dox gavage, (iv) C/A-bearing animals + control (water) gavage. Each line represents a single animal from time of implant to point of sacrifice. When tumours reached ~ 800 mm³, animals were given dox (daily gavage 0.2 mg/ml p.o) or water, represented by a dotted horizontal line. (v) Data from (i–iv) represented as mean \pm SEM (***P* < 0.001); solid black bars, revC3 + dox; open white bars, revC3 – dox; light grey bars, C/A + dox; hashed bars, C/A – dox; *n* = 7–10 animals per group. (b) Representative images of staining for cleaved caspase-3, cleaved PARP and caspase-cleaved CK18 as tissue biomarkers of apoptosis in RevC3 and C/A xenografts 24 h \pm dox (i). Quantitation of these data in comparison to the parental cell line (par) and tumour volumes (ii). Kinetics of revC3 tumor apoptosis in comparison to tumor volumes (iii): black line, tumor volume, solid black bars, cleaved caspase-3, open white bars, cleaved PARP, grey bars, caspase-cleaved CK18. Error bars represent \pm SEM, 2–4 mice per group, 2–5 sections per group, **P* < 0.02, 2 independent counts. (c) Correlation of circulating CK18 levels with tumor volumes (black line) in parental, revC3 and C/A xenograft-bearing mice (i). Kinetics of these changes in revC3 following dox (ii). Grey bars, total CK18; open white bars, caspase-cleaved CK18. Data shown are mean \pm SEM, 2–4 mice per group, ***P* < 0.01

tumour cell death *in vitro* and *in vivo* mapped, we then sought to demonstrate the utility of this model for biomarker discovery and validation using the complimentary approaches of proteomics and imaging.

Design and implementation of a proteomic workflow to assess early changes in the secretome of tumor cells triggered to undergo apoptosis. We recently developed a gel-free, proteomic workflow for relative quantification of proteins using iTRAQ labelling and tandem MS for analysis of samples such as conditioned media or plasma/serum

(Figure 3a).¹⁵ Figure 3b outlines the experimental design using this method, where changes in the identities and relative levels (up and down) of proteins secreted/released into the media of ‘death-switched’ cells after 6, 8 and 24 h were profiled as potential tumor death biomarkers. ProteinPilot identified 25 714 peptides. A *q*-value threshold of confidence > 0.29 (see Supplementary Material and ¹⁵) was applied resulting in 4657 peptides amongst which, 650 had reliable iTRAQ labelling. These peptides originated from 121 non-redundant proteins (identified with ≥ 2 peptides, Supplementary Table 1). The protein false discovery rate

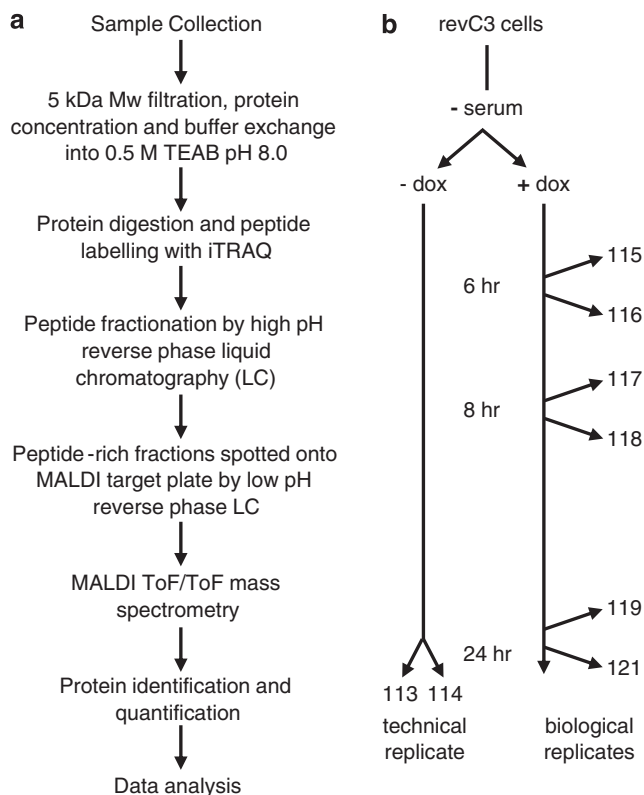


Figure 3 Proteomic workflow and experimental design to investigate apoptosis-related proteomic changes in the cell culture supernatant of ‘death-switched’ cells. (a) Gel-free proteomic workflow for relative quantitation of proteins using iTRAQ labelling and MS/MS mass spectrometry. (b) Experimental design to investigate proteomic changes in the cell culture supernatant of ‘death-switched’ cells. Numbers denote the iTRAQ tag designated for each sample in the proteomic analysis

(FDR) was 3.36%, thus protein identifications were deemed valid. Peptide and protein level variances are displayed in Supplementary Figure 1.

Technical variance was within acceptable limits of \log_2 0.85–1.27 (–0.24 to +0.34 after \log_2 transformation). Differentially expressed/present proteins following apoptosis induction were defined by boundaries representing 95% confidence intervals (CI) by assessment of variance between biological replicates at three different time-points. The upper and lower boundaries of CI were \log_2 0.65–1.49 (–0.62 to +0.57 after \log_2 transformation), resulting in 57/121 proteins present in media from cells at significantly altered levels at one or more time-points compared with non-apoptotic cells (Supplementary Figure 1, Table 1). Several of these were caspase substrates (Table 1, italic type), see Discussion. Of particular interest were fold changes occurring at early time-points (6 and 8 h); as during this period, >90% cells maintained plasma membrane integrity, although >70% demonstrated apoptotic nuclear morphology (Figures 1c (ii) and (iii), respectively). Differentially expressed proteins were grouped according to their normal subcellular localisation (<http://www.uniprot.org/>) (Table 1). Proteins were defined as secreted (17 proteins, 30% total differentially expressed), membrane-bound (11 proteins, 19% total), cytoplasmic (13 proteins, 23% total), nuclear (11 proteins, 19% total), or of unspecified location (5 proteins, 9% total). The secreted

proteins group was the largest, although all subcellular localisations were well represented.

Global protein increases and decreases were detected at all three time-points; interestingly, levels of secreted proteins all decreased and the majority of these (14/17) decreased at 6 h and remained so throughout the time course. In contrast, cytoplasmic proteins were found to be generally increased in the cell media (Table 1). Nuclear proteins were both increased and decreased and with the exception of HMGB1, HNRPA2 and Plasminogen Activator Inhibitor 1 RNA-binding Protein (elevated at 6 hour), the majority of changes occurred at 24 h. It must be noted that although CK18 was detected by the proteomics screen, it was not differentially expressed (see Discussion).

Several candidates were chosen for further validation, and western blotting for HMGB1, Heat Shock Protein 90 (Hsp90) and Nucleolin confirmed these increases, with Cytokeratin-8 as a loading control (detected in the proteomic screen with unchanged levels throughout) (Supplementary Table 1) (Figure 4a). Upregulation of CD44 was verified by ELISA (as western blotting was confounded due to the many splice variants of this protein) (Figure 4b). In agreement with proteomic data (Table 1), CD44 levels were significantly increased 24 h after induction of the death-switch (*t*-test, $P < 0.05$). These data indicate that the proteomics method adopted here is valid for biomarker discovery with demonstrable agreement for protein expression changes between different methodologies.

Analysis of tumor and plasma from mice bearing ‘death-switched’ tumors for novel circulating biomarkers of apoptotic tumor cell death.

The results generated by the *in vitro* proteomics screen were also corroborated in the plasma of mice bearing ‘death-switched’ tumors and as such could represent potential novel circulating biomarkers of apoptosis with demonstrable translational relevance. Substantially increased levels of HMGB1 were found in the plasma of these animals at 24 and 48 h (Figure 4c(i)). Furthermore, soluble CD44 was also increased at these time-points (Figure 4b(ii)). Early changes in HMGB1 observed in the proteomics screen were not found *in vivo* and it is possible that this reflects the more complex kinetics of release into the bloodstream *in vivo*. Interestingly, Figure 4c(i) appears to show several different isoforms of HMGB1, with at least two forms detectable in uninduced and 24- and 48-h post-dox time-points and possible other forms of intermediate size in the other time-points. This is in comparison to the single form of HMGB1 seen in the cell culture supernatant (Figure 4a). In order to investigate this further, HMGB1 in plasma from mice bearing death-switch tumours (or non-tumor bearing controls) was analysed by Nanofluidic proteomic immunoassay using the NanoPro1000 (ProteinSimple, Santa Clara, CA, USA). This technique separates native state proteins by isoelectric point before antibody detection. The signal from each time-point was subtracted from the background reading obtained from over the time course (Figure 4c(ii)). A more acidic form was present in the uninduced tumours (pI 4.6), which reduced to low levels at 24 h, at which point a less-acidic form (pI 6.5) could be detected, only present at 24 h. It is possible that this

Table 1 Proteins secreted into cell culture media with significant fold changes following induction of the death-switch after 6, 8 and 24 h

Protein Name	Fold change at each time-point post dox (log ₂)		
	6 h	8 h	24 h
<i>Secreted proteins</i>			
AGRN Agrin	-1.41	-1.40	-1.92
B2M Beta-2-microglobulin	-1.634	-1.66	-2.50
CST3 Cystatin-C	-1.57	-1.60	-2.34
GRN Granulins	-0.98	-1.07	-2.16
<i>GSN Gelsolin</i>	-1.14	-1.02	-1.74
HSPG2 Basement membrane-specific heparan sulfate proteoglycan core protein	-1.51	-1.52	-2.53
KLK6 Kallikrein-6	-0.90	-1.04	-2.03
LGALS3BP Galectin-3-binding protein	-1.03	-1.12	-1.21
THBS1 Thrombospondin-1	-1.06	-1.03	-1.61
TWSG1 Twisted gastrulation protein homolog 1	-0.99	-0.88	-1.85
SERPINA1 Alpha-1-antitrypsin	-1.43	-1.23	-2.06
LRG1 Leucine-rich alpha-2-glycoprotein	-0.650	1.00	-1.36
LYZ Lysozyme C	-1.44	-1.71	-1.80
SPINT1 Kunitz-type protease inhibitor 1	-0.14	-0.08	-0.58
HP Haptoglobin	0.16	0.20	-0.91
AMY1B Alpha-amylase 1	0.38	0.22	-1.20
MDK Midkine	-1.31	-1.26	-1.89
<i>Membrane proteins</i>			
ADAM17 Disintegrin and metalloproteinase domain-containing protein 17	-0.41	-0.83	-1.39
LSR Lipolysis-stimulated lipoprotein receptor	-1.08	-1.08	-1.99
SDC4 Syndecan-4	-0.58	-0.74	-1.36
SPINT2 Kunitz-type protease inhibitor 2	-0.49	-0.39	-0.71
SHISA5 Protein shisa-5	-1.73	-1.71	-2.91
EFNB1 Ephrin-B1	0.33	0.82	-0.07
ST14 Suppressor of tumorigenicity protein 14	0.09	0.31	1.15
GAPDH Glyceraldehyde-3-phosphate dehydrogenase	0.29	-0.06	1.17
*CD44 CD44 antigen	-0.44	0.41	0.82
DSG2 Desmoglein-2	-0.00	0.66	0.48
BCAM basal cell adhesion molecule precursor	0.08	0.64	0.82
<i>Cytoplasmic proteins</i>			
CTSH Cathepsin H	-0.72	-1.27	-2.56
HNRNPA2B1 Heterogeneous nuclear ribonucleoprotein 2B1	0.60	0.09	-0.32
<i>TUBA1B Tubulin-α-1B</i>	0.61	0.47	0.26
TMOD2 neuronal tropomodulin	0.66	0.77	0.07
S100A11 Protein S100-A11	0.33	0.07	-0.98
SERBP1 Plasminogen activator inhibitor 1 RNA-binding protein	0.65	0.21	0.18
GAPDH Glyceraldehyde-3-phosphate dehydrogenase	0.29	-0.06	1.17
*HSP90 heat shock 90kDa protein	0.26	0.21	0.64
*NCL Nucleolin	0.10	-0.03	1.16
PFN1 Profilin-1	-0.17	-0.39	0.65
PGK1 Phosphoglycerate kinase 1	0.25	-0.08	0.78
PKM2 Pyruvate kinase isozymes M1/M2	0.13	0.11	0.82
<i>SET Protein SET</i>	0.44	0.33	2.27
<i>Nuclear proteins</i>			
HIST1H1B Histone H1.5	0.10	0.12	-1.16
HIST1H1D Histone H1.3	0.21	0.16	-0.98
HIST1H1E Histone H1.4	-0.07	0.02	-0.91
HIST1H2BN Histone H2B type 1-N	0.27	0.23	-1.13
HNRNPA2B1 Heterogeneous nuclear ribonucleoprotein 2B1	0.60	0.09	-0.32
SERBP1 Plasminogen activator inhibitor 1 RNA-binding protein	0.65	0.21	0.18
S100A11 Protein S100-A11	0.33	0.07	-0.98
*HMGB1 High mobility group protein B1	0.66	0.39	0.89
*NCL Nucleolin	0.10	-0.03	1.16
PKM2 Pyruvate kinase isozymes M1/M2	0.13	0.11	0.82
<i>SET Protein SET</i>	0.44	0.33	2.27
<i>Proteins with unspecified location</i>			
ATIC Bifunctional purine biosynthesis protein PURH	0.62	0.56	0.22
SPINK5 Serine peptidase inhibitor	-0.82	-0.69	-1.77
MDH2 Malate dehydrogenase	0.04	-0.06	-0.96
<i>EEF1D Eukaryotic translation elongation factor 1 delta</i>	0.23	-0.02	0.67
TUBB3 Tubulin- β 3	0.80	0.61	0.79

Proteins identified in the *in vitro* proteomic screen with differential expression levels in serum-free media after death-switch induction, grouped by subcellular localization. Fold changes (compared with uninduced cells at 24 h) are expressed as log₂ values. Numbers that represent significant fold changes are in bold type. Proteins that were verified by alternative methods are in bold type and prefixed by an asterisk (HMGB1, Hsp90, CD44 and Nucleolin). Proteins in the CASBAH database⁷ are highlighted in italics (gelsolin, tubulin α -1-B, Hsp90, nucleolin, SET and eukaryotic elongation initiation factor 1 delta).

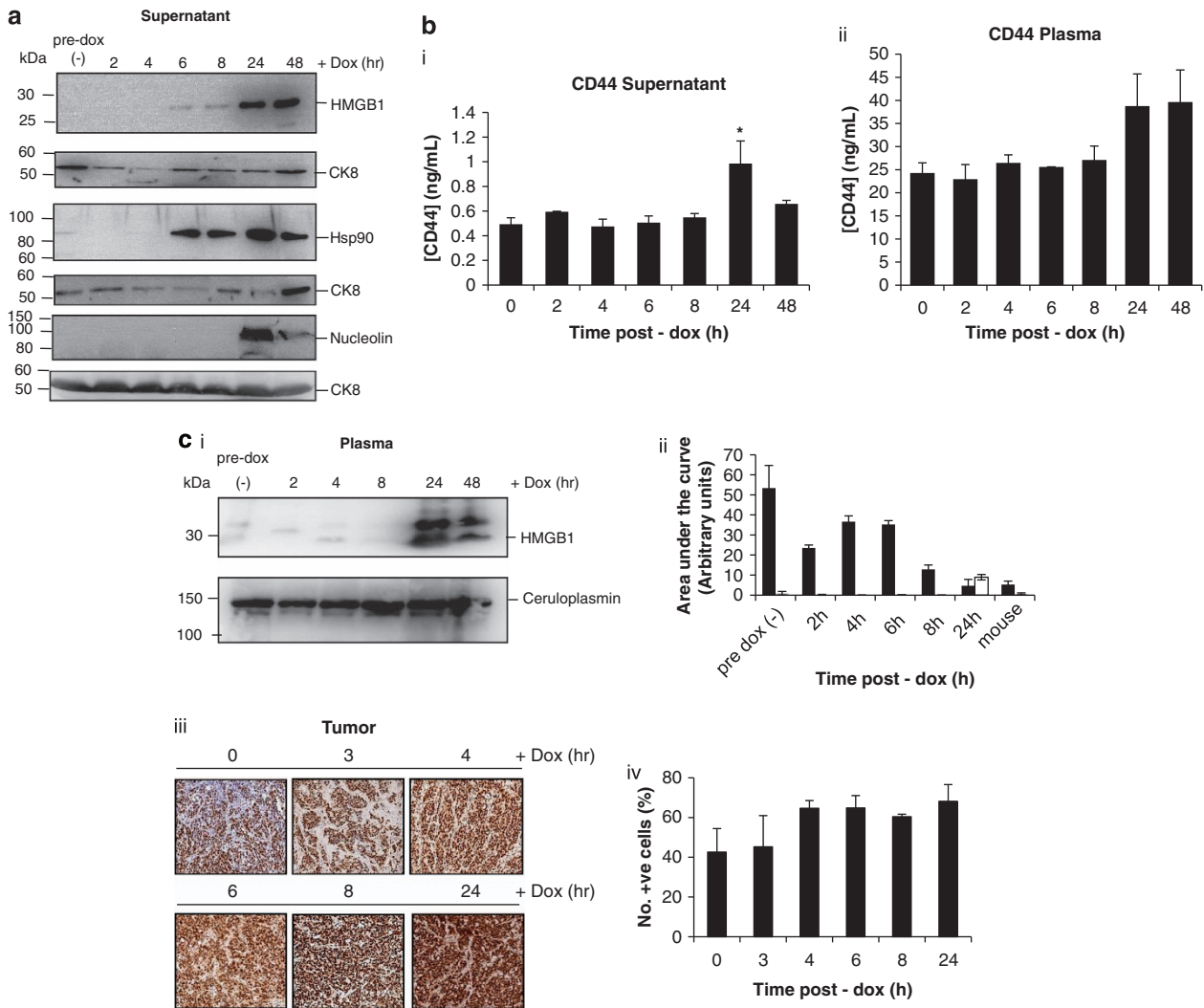


Figure 4 Verification of proteins that change in media of ‘death-switched’ cells, and in plasma of mice bearing ‘death-switched’ tumors. Cell media was examined before and after 4, 6, 8 and 24 h induction of revC3. Mouse plasma was evaluated from mice with revC3 xenografts, pre- and up to 24 h post induction of activated caspase-3. (a) Representative blots for HMGB1, Hsp90 and Nucleolin levels released into media with CK8 as a loading control (15 μ g total protein was loaded per lane). (b) CD44 (ELISA for total soluble CD44) released into cell media (i), $n=2$, mean \pm SD. * $P<0.05$ versus minus dox sample and mouse blood (ii) (plasma was pooled from 2–7 mice). (c) Representative blot for HMGB1 levels in mouse plasma with Ceruloplasmin as a loading control (i). Native protein isoelectric focusing of HMGB1 released into mouse plasma, $n=3$, mean \pm SD (plasma pooled from 2–7 mice) (ii). Representative images of staining for HMGB1 in death-switch xenografts over time (iii). Graphical representation of levels (%) of cytoplasmic HMGB1 staining from IHC of HMGB1 in xenografts from mice bearing death-switch tumors over time (iv), 2–4 mice per group, one-way ANOVA ($P=0.032$, trend analysis $P=0.003$) black bars, HMGB1 pH 4–5; open white bars, pH 6.45–6.5

second form is the source of the increased levels of HMGB1 observed in the western blot (Figure 4c(i)).

IHC analysis of HMGB1 was undertaken on the xenograft sections (Figure 4(iii)) and while there were no significant changes in nuclear HMGB1 expression (data not shown), analysis revealed significant changes in the expression of cytoplasmic HMGB1 post death-switch induction ($P=0.032$, one-way ANOVA). Under the ANOVA framework, a statistically significant linear trend over time was also observed ($P=0.003$) (Figure 4c(iv)).

Validation of [18 F]ML-10, an apoptotic imaging agent, using the death-switch tumour model. To demonstrate the use of the death-switch model for imaging biomarker validation, death-switch and control tumours were imaged

before and after induction of revC3 with [18 F] ML-10, the first PET apoptosis imaging agent to reach phase I/II clinical trials for the detection of cell death.⁹ There was a significant increase in [18 F] ML-10 uptake (NUVmean) at 24 h post therapy (2.61 ± 0.69 versus 1.40 ± 0.27 , $P<0.05$), which was not seen in the control group (2.19 ± 0.68 versus 1.77 ± 0.51) (Figures 5a–c); expression levels of cC3 and cPARP relative to actin were also increased as were circulating levels of M30 (data not shown). There was no significant difference in NUVmean between groups at baseline.

Discussion

In the era of molecularly targeted agents for cancer therapy, the need for biomarkers to monitor drug-induced changes in

tumors is clear. To this end, we developed and validated an inducible caspase-3 tumor ‘death-switch’ model, whereby human cancer cells undergo synchronous apoptosis *in vitro* and *in vivo* (Figures 1 and 2). The model avoids potentially confounding effects of alternative cell death mechanisms and non-synchronous kinetics of drug-induced cell death. It therefore provides an unique opportunity to identify cell death biomarkers of potential clinical relevance and facilitates examination of early changes in the microenvironment of cells destined to die.

Firstly, we demonstrated the use of this model for the identification of novel biomarkers by a proteomic study of cell culture media of death-switched cells. The proteomics platform we describe enabled identification of 57 proteins whose levels change in the media of cells undergoing apoptosis. Confirmed increases in the cell supernatant of HMGB1, Hsp90 and Nucleolin were shown by western blotting and increases in CD44 by ELISA (Figure 4a). CD44 (Figure 4b) and HMGB1 (Figures 4a and c) also increased in the bloodstream of mice bearing death-switched tumors and serve to validate our proteomics approach. In the proteomics screen, HMGB1 was increased at early (before loss of membrane integrity) and late time-points and its role in the dying cell microenvironment may differ depending on the kinetics of its release. Hyperacetylated HMGB1 is associated with inflammatory responses,^{16–18} and it is conceivable that a tumor cell destined for apoptosis might contribute to triggering the immune response. This hypothesis is being tested using a murine cell line engineered to express the death-switch, grown as a tumor in immune-competent mice.¹⁹ In addition to showing that this model is amenable to other cell lines, this study also showed HMGB1 and Hsp90 release and indicated their potential role as ‘danger signal’ molecules following apoptosis induction. Interestingly, Kroemer *et al.*²⁰ have previously shown that release of HMGB1 from tumor cells undergoing chemotherapy-induced cell death enhances immunogenic clearance. Hypoacetylated HMGB1 is released passively during necrosis, thus tumor cells undergoing synchronous ‘death-switched’ apoptosis at 24 h may have overwhelmed phagocytic clearance generating ‘secondary’ necrosis. Hyperacetylated HMGB1 has been shown to be redirected from the nucleus to the cytoplasm, for eventual secretion via exocytosis,²¹ and Figures 4c (iii) and (iv) shows increased expression of cytoplasmic HMGB1 does indeed increase significantly following activation of apoptosis *in vivo* (one-way ANOVA $P=0.032$, trend analysis $P=0.003$). Furthermore, at least two forms of soluble HMGB1 are present in mouse plasma following death-switch activation Figure 4c(ii), with a less acidic form being present only at the 24 h time-point, which suggests that different post-translational modifications are present depending upon the degree of apoptosis and/or necrosis that is present.

CD44 levels were elevated in the plasma of mice bearing death-switched xenografts at 24–48 h. CD44 is a class I transmembrane glycoprotein that can act as a receptor for extracellular matrix components, and is a downstream target of the Wnt/ β -catenin pathway.²² CD44 has been identified as a colorectal cancer stem cell marker and has been linked with more aggressive tumors.²³

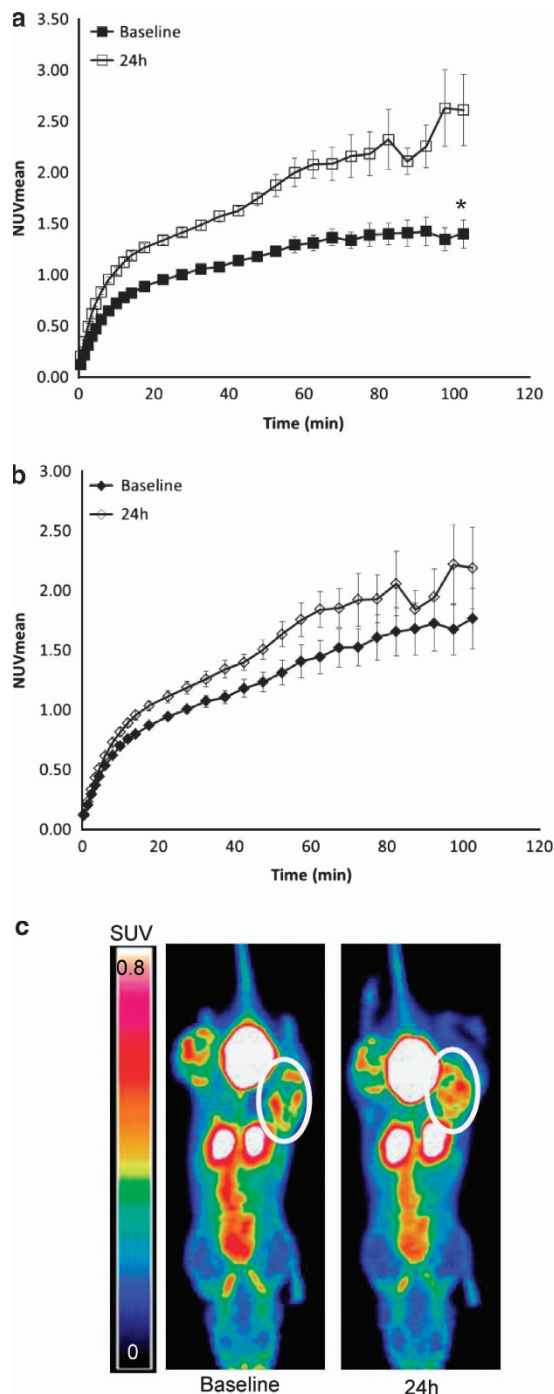


Figure 5 Uptake of the apoptotic PET tracer [^{18}F]ML-10 increases in ‘death-switch’ versus control tumours. Average maximum normalized uptake time activity curves for revC3 xenografts at baseline (closed symbol) and after 24 h treatment with doxycycline (open symbol) (average \pm SEM, $*P < 0.05$) (a) Average maximum normalized uptake time activity curves for C/A xenografts at baseline (closed symbol) and after 24 h treatment with doxycycline (open symbol) (average \pm SEM.) (b) Maximum intensity projections from summed 30–35 min PET data showing uptake of [^{18}F]ML-10 in revC3 (circled) and C/A xenografts in a representative animal at baseline and 24 h after doxycycline treatment (c)

This study also prompted the hypothesis that changes in released/secreted proteins from cells during the early stages of apoptosis might not be inconsequential. At early time-points,

although cells are destined to die, plasma membrane integrity was maintained (Figure 1c), which may indicate protein changes that occur in an orchestrated rather than passive manner and that intracellular events during apoptosis may direct secretion of specific proteins that have an impact on the behaviour of surrounding viable cells. There is evidence that caspase-mediated cellular demolition is not indiscriminate and effector caspases selectively cleave components of biochemical pathways critical for cell viability.^{7,24,25}

Several proteins whose expression changed in the media of death-switched cells *in vitro* (Figure 3 and Table 1) were present in the caspase substrate database, CASBAH⁷ (Table 1, proteins in italic type). Two of these *bona fide* caspase substrates, Hsp90 and Nucleolin, have verified caspase-cleavage sites and were also found to be increased in media 24 h after death-switch induction. Both were detectable by western blot in the media of these cells, with apparent peaks at 24 h, concurrent with proteomics data (Figure 4a and Table 1), although Hsp90 was detected by western blot as early as 6 h post death-switch induction. Extracellular Hsp90 is linked to immune stimulation,²⁶ while Nucleolin acts as macrophage receptor for apoptotic cells,²⁷ thus potentially explaining its increased expression during apoptosis induced by the death-switch.

The majority of proteins decreased in the media of death-switched cells and for many this occurred early (from 6 h) (Table 1). Some of these proteins are associated with apoptosis and tumorigenesis (e.g. leucine-rich α -2 glycoprotein and thrombospondin-1),^{28,29} but many are not and are potential novel biomarkers of cell death warranting further characterisation. Furthermore, decreases in levels of these secreted proteins did not appear to correlate with protein half-life, suggesting an 'orchestrated' role in cellular responses to apoptotic cell death. While CK18 was identified by the proteomics screen at all time-points, somewhat unexpectedly, its levels were not found to change significantly. This can be explained by the greater sensitivity of ELISA/antibody-based methods compared with the mass spec approach used here.³⁰ While the iTRAQ method has many advantages as a global discovery approach,³¹ it is limited by underestimation of fold changes.³² Additionally, both these methods do not provide absolute quantitation, and thus, CK18 may be below the limit of detection of this mass spec method.

Secondly, we established the utility of this model for the validation of apoptosis imaging biomarkers using [¹⁸F]ML-10, a PET tracer. Existing *in vivo* models of apoptosis include the induction of hepatocytic cell death by systemic administration of drugs, or the treatment of sensitive tumor xenograft models with chemo- or radiotherapy,³³ but these suffer from both the severity of the procedure to the host animal, as well as the inherent variability of apoptotic response to stimuli. The synchronous and well-tolerated induction of cell death in this model is helpful for the validation of PET imaging biomarkers *in vivo*, as this variability is reduced; it also allows the comparison of longitudinal changes in tracer uptake in tumors undergoing cell death with control tumors in the same animal, where the pharmacokinetics of tracer delivery are identical. Our results show increased uptake of [¹⁸F]ML-10 in tumors undergoing apoptosis as previously reported *in vitro*³⁴ and in

other apoptotic models *in vivo*,³⁵ although the overall level was not as pronounced as reported for the related compound ML-9 *in vivo*.³⁶

In summary, the need for non-invasive biomarkers for clinical use is clear. In the era of novel targeted therapies to promote tumour apoptosis for the treatment of cancer, the need for accurate, robust and controllable model systems to test these drugs and modalities is also evident. Our preclinical death-switch model allows tightly controlled induction of apoptosis *in vivo* with demonstrable application for the discovery and validation of biomarkers of cell death.

Materials and Methods

Molecular biology. The cDNAs encoding revC3 and revC3 containing a C to A point mutation within the active site (revC3 C/A)⁸ were inserted into the multiple cloning site of pTRE2hyg (Clontech, Laboratories Inc., Mountain View, CA, USA) to generate pTREhygRevC3 and pTRE2hygRevC3 C/A.

Cell culture. HT29 CCE9 cells were cultured as described previously.¹¹ To generate revC3 and C/A clones, cells were electroporated with 20 μ g pTRE2hygRevC3 or pTRE2hygRevC3 C/A, respectively and cultured in the presence of 500 μ g/ml hygromycin (Sigma, Sigma-Aldrich Ltd., Gillingham, UK) in 10 cm² dishes for ~2 weeks and ~100 discrete colonies picked when visible.³⁷ RevC3 and revC3 C/A expression was induced with 2 μ g/ml doxycycline (dox) (Clontech) and clones were screened for revC3 and revC3 C/A expression and activity by western blotting and for viability by trypan blue exclusion.

Cell viability assays. The sulforhodamine B (SRB) assay was used to determine cell population number \pm 2 μ g/ml dox.³⁸ Cells were plated in exponential growth phase in 96-well plates \pm dox and at daily intervals for 7 days cells prior to SRB assay. Viability assays was assessed by standard trypan blue dye exclusion.

Fluorometric caspase-3 activity assay. Cells were seeded in six-well plates at 1×10^6 cells/well and 24 h later, cells were incubated \pm dox before harvesting after 2, 6 and 24 h. Cell pellets were resuspended in Caspase-3 Buffer \pm Caspase-3 Substrate II DEVD-AMC, \pm Caspase Inhibitor DEVD-CHO (10 mM stock in DMSO) (R&D Systems, Abingdon, UK).³⁹ Enzyme activity was determined after 45 min at 505 nm (emission) on a Fluostar Optima fluorescence plate reader (BMG Labtechnologies, Aylesbury, UK). All data were corrected for cell number.

Microscopy. Nuclear apoptotic morphology was assessed by fluorescence microscopy of fixed cells stained with DAPI.⁴⁰

Tumor xenografts. RevC3, revC3 C/A and parental cell xenografts were grown by s.c injection of 1×10^7 cells (0.1 ml of serum-free medium) into the back mid-dorsal region of 6–8-week-old SCID/*bg* mice, either a single or dual flank (different cell lines injected on opposite flanks) model (Paterson Institute for Cancer Research). For growth and cell death kinetics, the study mice were housed and tumor size monitored, as previously described,⁴⁰ until 800 mm³ at which point, tail vein bleeds were taken. Animals received either dox or water by gavage (0.2 ml p.o., 10 mg/ml) every 24 h for 5 days or until tumors reached 1250 mm³, whichever occurred sooner. On sacrifice or bleeding, blood was collected into heparinised tubes and plasma was prepared.⁴¹ For cell death kinetics studies, mice were randomised when tumors reached ~800 mm³ and pre-dox tail vein bleeds were taken. At various time-points, mice were culled, and bloods and tumors collected.⁴⁰ For imaging studies, mice were implanted as previously described using a dual flank model, and after 17 days animals were selected for imaging based on having paired size-matched tumours of 300 mm³ (within 25%) before receiving one dose of dox prepared as described above. All procedures were carried out in accordance with the Scientific Procedures Act 1986 and UKCCR Guidelines 2010 by approved protocols following institutional guidelines (Home Office Project Licence 40-3306 held by Professor C Dive).

Immunohistochemistry. IHC for cleaved caspase-3, cleaved PARP and caspase-cleaved CK18 was carried out as previously described,⁴² using the following primary antibodies: cleaved caspase-3 (Cell Signaling Technology, Danvers, MA, USA Asp175, product number 9661 1 : 200 dilution), cleaved PARP

(BD Pharmingen, Oxford, UK Asp214, product number 51-900017 1:100 dilution), M30 (Peviva Bromma, Sweden product number 10700 1:100 dilution) and HMGB1 (AbCam, Cambridge, UK, product number ab18256 1:100 dilution). Control tissue was MDA-231 XG4 breast carcinoma cells⁴³ \pm 1 μ M staurosporin. The negative control rabbit IgG was as follows: cleaved caspase-3, 1:25000 (DakoCytomation, Glostrup, Denmark, product number X0936), cleaved PARP, 1:20 (DakoCytomation, product number X0931), M30, 1:100 (DakoCytomation, product number X0944). Staining was quantitated as follows: digital images of whole-tissue sections were acquired using a Leica SCN400 histology scanner (Leica Microsystems, Milton Keynes, UK). Ten images from each slide were selected at random at \times 20 magnification using Mirax Viewer software. The total number of cells per area was determined using the 'nucleus counter' plug-in for ImageJ software and the number of positive cells per section was counted by two blinded, independent counters before averaging the data. In the case of HMGB1, 5 μ m-thick formalin-fixed paraffin-embedded sections were dried for 1 h in a 60 °C oven. Staining was performed using the BondMax autostainer and reagents (Leica Microsystems). Deparaffinization was performed automatically in the autostainer with BondDewax solution at 72 °C for 30 min followed by 3 rinses in each of reagent alcohol and BondWash solution. Slides were then incubated with Epitope Retrieval Solution 1 (Leica Microsystems, Wetzlar, Germany) for 20 min at 100 °C, peroxide block for 5 min. IHC was performed using a pAB against HMGB1 (1:200, 18256, Abcam). Antigen was visualized using the EnVision kit (Dako, Glostrup, Denmark) for 60 min. Positive controls included in each run were tonsil sections positive for HMGB1. Negative controls for each tissue section were treated the same as test slides with RIgG antibody, dilution 1:1000. Images were analysed using Definiens Developer XD version 2.0.4 and the Tissue Studio Portal version 3.51 (Definiens AG, Munich, Germany). Regions of interest (ROIs) within the tissue sections were first identified using Definiens Tissue Studio via machine learning technology across several samples so that the full range of contrast was defined. Within these ROIs, nuclei were detected and classified as positive or negative based on haematoxylin and HMGB1 staining thresholds. Cells were subsequently simulated around all nuclei and classified as positive or negative based on thresholds set for the HMGB1 stain within the cytoplasm. All thresholds remained consistent across tissue sections. For all IHC, 2–4 animals were used at each time-point. One-way analysis of variance (ANOVA) was applied to HMGB1 staining in xenograft sections, including linear trend analysis under the ANOVA framework (SPSS Software).

Western blotting. Western blotting was performed, as previously described,⁴⁰ using the following antibodies: cleaved caspase-3 (Cell Signaling Technology Asp175, product number 9661, 1:100 dilution) and PARP (Cell Signaling Technology, product number 9542, 1:1000 dilution), tubulin (Abcam, product number ab4074, 1:3000 dilution), actin (Sigma, product number a3853, 1:2500 dilution), HMGB1 (Abcam, product number ab18256, 1:1000 dilution), Cytokeratin-8 (Sigma, product number C5301 1:100 dilution), Ceruloplasmin (Sigma, product number GW20074F, 1:500 dilution), Hsp90 (Enzo Life Sciences, product number ADI-SPA-846-D, 1:1000 dilution) and Nucleolin (AbCam, product number ab13541, 1:1000 dilution). In the case of cell culture supernatants, 12% SDS-PAGE gels were used, while 4–12% gradient gels (Invitrogen, Paisley, UK) were used for the mouse plasma.

M30/M65 ELISA. ELISA assay for relative quantitation of soluble intact CK18 (M65) and caspase-cleaved CK18 (M30) was carried out on cell culture supernatant according to the manufacturer's instructions (Peviva). In the case of mouse plasma 4 μ l Heterophilic Blocking Reagent (HBR Plus, Scantibodies Laboratory, Inc., Santee, CA, USA) was added to each well and assays were carried out as previously described.⁴¹

CD44 ELISA. ELISA assay for quantitative determination of soluble CD44 in serum, plasma, buffered solutions and cell culture supernatant (Abcam, Cat #45912) was carried out according to the manufacturer's instructions.

Nanofluidic proteomic immunoassay. The total protein concentration of plasma from SCID/*bg* mice bearing xenografts of revC3 at 800 mm³ (minus dox) or following dox (2, 4, 6, 8 and 24 h) or non-tumour-bearing control mice (SCID/*bg*) was determined using a Bradford assay (Biorad, Hercules, CA, USA). Protein concentration was then normalised to 2 μ g/ μ l using water. In all the following procedures, sample reagents were from Protein Simple unless otherwise stated. One microlitre of the mixture was diluted to 200 ng/ μ l with sample diluent

containing 2% DMSO inhibitor mix. The sample was then further diluted with 30 μ l of Premix G2 pH 5–8 (nested) separation gradient containing pI standard ladder 1. Four hundred nanolitres of this mix was then separated by isoelectric point using the NanoPro1000 (Protein Simple) using the power 1 step separation profile, 100 s immobilisation exposure and 480 min primary incubation. HMGB1 antibody (AbCam, product number ab18256) was used at 1:100 dilution. Data were initially analysed using the NanoPro1000 software, Compass version 1.81, to extract the raw spectra from the two pI regions 4–5 and 6.45–6.55 as a text. These regions were selected based on their specificity when compared with non-tumour bearing control mice. MedCalc (version 12.3.0.0; Ostend, Belgium) was then used to calculate the area under the curve for each of the samples over the two pI regions. All analysis was carried out in triplicate, and averages and SD are shown.

Experimental design for proteomics experiments. An overview of the complete workflow is shown in Figure 3a.

Cell growth and media preparation for proteomics. 1×10^6 revC3 cells were seeded into T25 flasks (described above), after 24 h culture medium was removed and cells were washed before incubation with McCoy's 5A medium minus fetal bovine serum. After 6, 8 and 24 h + dox, medium from duplicate flasks was removed (to provide biological replicates) and after 24 h media from an additional flask minus dox was also harvested. This sample was split, creating two technical replicates and processed independently to allow for experimental variability to be assessed. Cellular debris were removed by centrifuging (500 \times g, 5 min) and samples stored at –80 °C. Samples were concentrated (~1 mg/ml final) and buffer exchanged into 1M TEAB using Vivaspin centrifugal concentrators (VS0413, Sartorius, Epsom, UK) as per the manufacturer's instructions (Figure 3b).

Protein digestion and iTRAQ labelling. Preparation of samples for proteomics was as previously described.⁴⁴

High pH reverse phase chromatography. iTRAQ-labelled samples were reconstituted in 100 μ l of 0.1% ammonium hydroxide and pooled prior to loading onto a 100 \times 4.6 mm, 3 μ m C18 HPLC column (Fortis, Cheshire, UK). Peptides were eluted by addition of a linear 30 min gradient up to 50% acetonitrile, 0.1% ammonium hydroxide with 70 \times 15 s fractions collected from 4 min. Fractions were dried in a SpeedVac (ThermoFisher Scientific, Loughborough, UK) at 60 °C and stored at –20 °C.

LC/MS/MS. Samples were reconstituted in 130 μ l of 0.1% Trifluoroacetic acid (TFA), 2% acetonitrile. Half was loaded onto a trap column using a U3000 liquid chromatography system (Dionex, Sunnyvale, CA, USA) and peptides fractionated with a capillary RP C18 HPLC column (Acclaim PepMap C18, 3 μ m 100 Å), flow rate 0.8 μ l/min, 2–40% acetonitrile, 0.1% TFA. The flowthrough was spotted onto a MALDI plate (AB SCIEX, Foster City, CA, USA) in 15 s fractions using an online Probot (Dionex) with α -cyano-4-hydroxycinnamic acid mixing with eluent, final concentration 1.25 mg/ml. Mass spectrometry was on an AB SCIEX TOF/TOF 5800 (AB SCIEX, Framingham, MA, USA) using 1000 shots for MS. MS/MS was applied to the top 27 precursors with a S/N of >8 using 4000 laser shots, a 2-KV acceleration voltage and air as collision gas.

Protein database searching and false discovery rate calculation. Proteins were identified using ProteinPilot v3.0 (AB Sciex) against the IPI Human (v3.59) protein sequence database as described in.⁴³ FDR determination and protein quantification are described in detail in the Supplementary material and follows a *q*-value-based statistical approach as previously described.¹⁵

Radiochemical synthesis of [¹⁸F]JML-10. A novel multi-step synthesis of ML-10 was developed in-house (Kadirvel M, Brown G; manuscript submitted). The radiochemical synthesis of di-*tert*-butyl ester of [¹⁸F]JML-10 was prepared by Kryptofix (Sigma-Aldrich, Gillingham, UK)-mediated nucleophilic fluorination of the mesylate group of di-*tert*-butyl 2-methyl-2-(5'-(methylsulfonyloxy)pentyl)malonate. Finally, deprotection of di-*tert*-butyl ester of [¹⁸F]JML-10 by acid hydrolysis gave [¹⁸F]JML-10. Isolation of pure [¹⁸F]JML-10 was achieved by semi-preparative reverse phase HPLC. The radiochemical synthesis used the FX-FN platform (GE Healthcare, Chalfont-St Giles, UK). The radiochemical yield (decay-corrected) of [¹⁸F]JML-10 from nucleophilic [¹⁸F]fluoride was 26–31%, giving 4.54–5.79 GBq of product at the end of the radiosynthesis (EOS). The radiochemical purity was

≥99%, and the specific radioactivity was 25.3–29.2 GBq mol⁻¹ (EOS). The total radiosynthesis time was ~80 min.

PET imaging. Animals underwent dynamic baseline scanning when xenograft size had reached ~200–300 mm³ for subcutaneous tumors. Animals were anaesthetised with 1–2% Isoflurane, the tail vein was catheterised and they were placed in the animal bed (Equipment Veterinaire Minerve, Esternay, France) and transferred to a preclinical PET scanner (Inveon, Siemens, Malvern, PA, USA). At the start of the acquisition, mice were injected with 30–70 MBq of [¹⁸F]ML-10 (synthesised 'in-house' using published protocols⁴¹) intravenously (IV) via the tail vein. List mode data were collected for 105 min, in accordance with maximal acquisition times advised.⁴⁵ Anaesthesia was maintained during image acquisition via a nose cone, with respiration and temperature monitored throughout using appropriate systems. After imaging, animals were recovered in a warmed chamber, randomized into treatment groups and rescanned at 24 h after induction of revC3 with doxycycline. Immediately after the last scan, the tumors were excised, weighed and half-fixed in 10% formalin, and half snap-frozen in liquid nitrogen for western blot analysis.

Image reconstruction and data analysis. Before reconstruction, the list-mode data were histogrammed with a span of 3 and maximum ring differences of 79 into 3D sinograms with 21–33 time frames (5 × 60 s (s), 5 × 120 s, 5 × 300 s and 6 to 18 × 300 s) for image reconstruction. Images were reconstructed using the 3D-OSEM/MAP algorithm (4 OSEM3D iterations and no MAP iterations, with a requested resolution of 1.5 mm). ROIs were drawn manually over tumor and a section of liver using Inveon Research Workplace software (Siemens, Germany) and further normalization was performed using the injected dose (from the dose calibrator) and animal weight to give a standardized uptake value (SUV). SUVmean was calculated as the average over all voxels, with normalized uptake values (NUV) calculated by dividing SUVmean from the tumor by that from the liver contents.

Statistical tests. Unless otherwise stated, *P*-values are derived from Student's *t*-test.

Conflict of Interest

The authors declare no conflict of interest.

Acknowledgements. CD, KLS, CZ, CLS, FT and MJD are funded by Cancer Research UK (Paterson Institute for Cancer Research Core Funding from Grant Code: C147/A12328, Clinical Research Initiative Grant Code: C357/A12197). CC is funded by the Manchester Cancer Research Centre. MW is funded by Experimental Cancer Medicines Centre Grant. MM is funded by the Medical Research Council, UK (Intramural Grant in Aid Code MCA600). ADW is funded by Leukaemia Lymphoma Research UK (LRF code 08004).

1. Hanahan D, Weinberg RA. The hallmarks of cancer. *Cell* 2000; **100**: 57–70.
2. Taylor K, Micha D, Ranson M, Dive C. Recent advances in targeting regulators of apoptosis in cancer cells for therapeutic gain. *Expert Opin Investig Drugs* 2006; **15**: 669–690.
3. Letai AG. Diagnosing and exploiting cancer's addiction to blocks in apoptosis. *Nat Rev Cancer* 2008; **8**: 121–132.
4. Creagh EM, Conroy H, Martin SJ. Caspase-activation pathways in apoptosis and immunity. *Immunol Rev* 2003; **193**: 10–21.
5. Nicholson DW. Caspase structure, proteolytic substrates, and function during apoptotic cell death. *Cell Death Differ* 1999; **6**: 1028–1042.
6. Thornberry NA, Lazebnik Y. Caspases: enemies within. *Science* 1998; **281**: 1312–1316.
7. Luthi AU, Martin SJ. The CASBAH: a searchable database of caspase substrates. *Cell Death Differ* 2007; **14**: 641–650.
8. Srinivasula SM, Ahmad M, MacFarlane M, Luo Z, Huang Z, Fernandes-Alnemri T *et al*. Generation of constitutively active recombinant caspases-3 and -6 by rearrangement of their subunits. *J Biol Chem* 1998; **273**: 10107–10111.
9. Allen AM, Ben-Ami M, Reshef A, Steinmetz A, Kundel Y, Inbar E *et al*. Assessment of response of brain metastases to radiotherapy by PET imaging of apoptosis with (18F)-ML-10. *Eur J Nucl Med Mol Imaging* 2012; **39**: 1400–1408.
10. Hoglund J, Shirvan A, Antoni G, Gustavsson SA, Langstrom B, Ringheim A *et al*. 18F-ML-10, a PET tracer for apoptosis: first human study. *J Nucl Med* 2011; **52**: 720–725.

11. Welman A, Cawthorne C, Barraclough J, Smith N, Griffiths GJ, Cowen RL *et al*. Construction and characterization of multiple human colon cancer cell lines for inducibly regulated gene expression. *J Cell Biochem* 2005; **94**: 1148–1162.
12. Kramer G, Erdal H, Mertens HJ, Nap M, Mauermann J, Steiner G *et al*. Differentiation between cell death modes using measurements of different soluble forms of extracellular cytokeratin 18. *Cancer Res* 2004; **64**: 1751–1756.
13. Biven K, Erdal H, Hagg M, Ueno T, Zhou R, Lynch M *et al*. A novel assay for discovery and characterization of pro-apoptotic drugs and for monitoring apoptosis in patient sera. *Apoptosis* 2003; **8**: 263–268.
14. Hagg M, Biven K, Ueno T, Rydlander L, Bjorklund P, Wiman KG *et al*. A novel high-throughput assay for screening of pro-apoptotic drugs. *Invest New Drugs* 2002; **20**: 253–259.
15. Zhou C, Simpson KL, Lancashire LJ, Walker MJ, Dawson MJ, Unwin RD *et al*. Statistical considerations of optimal study design for human plasma proteomics and biomarker discovery. *J Proteome Res* 2012; **11**: 2103–2113.
16. Lotze MT, Tracey KJ. High-mobility group box 1 protein (HMGB1): nuclear weapon in the immune arsenal. *Nat Rev Immunol* 2005; **5**: 331–342.
17. Muller S, Scaffidi P, Degryse B, Bonaldi T, Ronfani L, Agresti A *et al*. New EMBO members' review: the double life of HMGB1 chromatin protein: architectural factor and extracellular signal. *EMBO J*. 2001; **20**: 4337–4340.
18. Antoine DJ, Williams DP, Kipar A, Jenkins RE, Regan SL, Sathish JG *et al*. High-mobility group box-1 protein and keratin-18, circulating serum proteins informative of acetaminophen-induced necrosis and apoptosis in vivo. *Toxicol Sci* 2009; **112**: 521–531.
19. MHM Melis, Simpson KL, Dovedi SJ, Welman A, MacFarlane M, Dive C, Honeychurch J, Ildige T. Sustained tumour eradication after induced caspase-3 activation and synchronous tumour apoptosis requires an intact host immune response. *Cell Death and Differ* 2013; **20**: 774–783.
20. Zitvogel L, Kroemer G. Anticancer immunotherapy using adjuvants with direct cytotoxic effects. *J Clin Invest* 2009; **119**: 2127–2130.
21. Bonaldi T, Talamo F, Scaffidi P, Ferrera D, Porto A, Bachi A *et al*. Monocytic cells hyperacetylate chromatin protein HMGB1 to redirect it towards secretion. *EMBO J*. 2003; **22**: 5551–5560.
22. Negi LM, Talegaonkar S, Jaggi M, Ahmad FJ, Iqbal Z, Khar RK. Role of CD44 in tumour progression and strategies for targeting. *J Drug Target* 2012; **20**: 561–573.
23. Lugli A, Iezzi G, Hostettler I, Muraro MG, Mele V, Tornillo L *et al*. Prognostic impact of the expression of putative cancer stem cell markers CD133, CD166, CD44s, EpCAM, and ALDH1 in colorectal cancer. *Br J Cancer* 2010; **103**: 382–390.
24. Dix MM, Simon GM, Cravatt BF. Global mapping of the topography and magnitude of proteolytic events in apoptosis. *Cell* 2008; **134**: 679–691.
25. Mahrus S, Trinidad JC, Barkan DT, Sali A, Burlingame AL, Wells JA. Global sequencing of proteolytic cleavage sites in apoptosis by specific labeling of protein N termini. *Cell* 2008; **134**: 866–876.
26. Joly AL, Wettstein G, Mignot G, Ghiringhelli F, Garrido C. Dual role of heat shock proteins as regulators of apoptosis and innate immunity. *J Innate Immun* 2010; **2**: 238–247.
27. Hirano K, Miki Y, Hirai Y, Sato R, Itoh T, Hayashi A *et al*. A multifunctional shuttling protein nucleolin is a macrophage receptor for apoptotic cells. *J Biol Chem* 2005; **280**: 39284–39293.
28. Codina R, Vanasse A, Kelekar A, Vezys V, Jemmerson R. Cytochrome c-induced lymphocyte death from the outside in: inhibition by serum leucine-rich alpha-2-glycoprotein-1. *Apoptosis* 2010; **15**: 139–152.
29. Friedl P, Vischer P, Freyberg MA. The role of thrombospondin-1 in apoptosis. *Cell Mol Life Sci* 2002; **59**: 1347–1357.
30. Zhi W, Wang M, She JX. Selected reaction monitoring (SRM) mass spectrometry without isotope labeling can be used for rapid protein quantification. *Rapid Commun Mass Spectrom* 2011; **25**: 1583–1588.
31. Simpson KL, Whetton AD, Dive C. Quantitative mass spectrometry-based techniques for clinical use: biomarker identification and quantification. *J Chromatogr B Analyt Technol Biomed Life Sci* 2009; **877**: 1240–1249.
32. Ow SY, Salim M, Noirel J, Evans C, Rehman I, Wright PC. iTRAQ underestimation in simple and complex mixtures: 'the good, the bad and the ugly'. *J Proteome Res* 2009; **8**: 5347–5355.
33. De Saint-Hubert M, Prinsen K, Mortelmans L, Verbruggen A, Mottaghy FM. Molecular imaging of cell death. *Methods* 2009; **48**: 178–187.
34. Cohen A, Shirvan A, Levin G, Grimberg H, Reshef A, Ziv I. From the Gla domain to a novel small-molecule detector of apoptosis. *Cell Res* 2009; **19**: 625–637.
35. Reshef A, Shirvan A, Waterhouse RN, Grimberg H, Levin G, Cohen A *et al*. Molecular imaging of neurovascular cell death in experimental cerebral stroke by PET. *J Nucl Med* 2008; **49**: 1520–1528.
36. Grimberg H, Levin G, Shirvan A, Cohen A, Yogev-Falach M, Reshef A *et al*. Monitoring of tumor response to chemotherapy in vivo by a novel small-molecule detector of apoptosis. *Apoptosis* 2009; **14**: 257–267.
37. Welman A, Barraclough J, Dive C. Generation of cells expressing improved doxycycline-regulated reverse transcriptional transactivator rTA2S-M2. *Nat Protoc* 2006; **1**: 803–811.
38. Vichai V, Kirtikara K. Sulforhodamine B colorimetric assay for cytotoxicity screening. *Nat Protoc* 2006; **1**: 1112–1116.

39. Rano TA, Timkey T, Peterson EP, Rotonda J, Nicholson DW, Becker JW *et al*. A combinatorial approach for determining protease specificities: application to interleukin-1beta converting enzyme (ICE). *Chem Biol* 1997; **4**: 149–155.
40. Martin-Fernandez C, Bales J, Hodgkinson C, Welman A, Welham MJ, Dive C *et al*. Blocking phosphoinositide 3-kinase activity in colorectal cancer cells reduces proliferation but does not increase apoptosis alone or in combination with cytotoxic drugs. *Mol Cancer Res* 2009; **7**: 955–965.
41. Micha D, Cummings J, Shoemaker A, Elmore S, Foster K, Greaves M *et al*. Circulating biomarkers of cell death after treatment with the BH-3 mimetic ABT-737 in a preclinical model of small-cell lung cancer. *Clin Cancer Res* 2008; **14**: 7304–7310.
42. Barraclough J, Hodgkinson C, Hogg A, Dive C, Welman A. Increases in c-Yes expression level and activity promote motility but not proliferation of human colorectal carcinoma cells. *Neoplasia* 2007; **9**: 745–754.
43. Cummings J, Ward TH, LaCasse E, Lefebvre C, St-Jean M, Durkin J *et al*. Validation of pharmacodynamic assays to evaluate the clinical efficacy of an antisense compound (AEG 35156) targeted to the X-linked inhibitor of apoptosis protein XIAP. *Br J Cancer* 2005; **92**: 532–538.
44. Pierce A, Unwin RD, Evans CA, Griffiths S, Carney L, Zhang L *et al*. Eight-channel iTRAQ enables comparison of the activity of six leukemogenic tyrosine kinases. *Mol Cell Proteomics* 2008; **7**: 853–863.
45. Workman P, Aboagye EO, Balkwill F, Balmain A, Bruder G, Chaplin DJ *et al*. Guidelines for the welfare and use of animals in cancer research. *Br J Cancer* 2010; **102**: 1555–1557.



Cell Death and Disease is an open-access journal published by **Nature Publishing Group**. This work is licensed under a Creative Commons Attribution-NonCommercial-NoDerivs 3.0 Unported License. To view a copy of this license, visit <http://creativecommons.org/licenses/by-nc-nd/3.0/>

Supplementary Information accompanies this paper on Cell Death and Disease website (<http://www.nature.com/cddis>)